Chapter 4

The Roman Pot system

4.1 System strategy and overview

The detection of very forward protons in movable beam insertions — called Roman Pots (RP) — is an experimental technique introduced at the ISR [10]. It has been successfully employed in other colliders like the S$\bar{p}$pS, TEVATRON, RHIC and HERA. Detectors are placed inside a secondary vacuum vessel, called a pot, and moved into the primary vacuum of the machine through vacuum bellows. In this way, the detectors are physically separated from the primary vacuum which is thus preserved against an uncontrolled out-gassing of the detector's materials.

The challenging constraints of the LHC, such as the thin high-intensity beam, the Ultra High Vacuum and the high radiation fluxes have required the development of new Roman Pots. The main differences to RPs designed for earlier machines lie in the window technology of the pots, which have to be placed much closer to the beam, and in the driving mechanism, which must have high precision and radiation hardness.

Being symmetric with respect to IP5, TOTEM's RP system allows the reconstruction of protons on both sides of the interaction point. On each side, two stations of Roman Pots will be mounted on the beam pipe of the outgoing beam. Their positions have been defined in an interplay with the development of the special optics used by TOTEM, with constraints given by the space available between the LHC machine components. The centre of the first station ('RP147') is placed at 149.6 m from IP5, and the second ('RP220') at 217.3 m. Between the two stations, the dipole magnet D2 provides a dispersion difference which helps in proton momentum reconstruction. To have a lever arm for local track reconstruction and trigger selections by track angle, each RP station is composed of two units separated by a distance limited by integration constraints with the other beam elements (figure 4.1). The stations RP147 and RP220 span distances of 1.2 m and 5 m respectively. Each RP unit consists of 3 pots, 2 approaching the beam vertically and 1 horizontally. A schematic drawing of the beam-pipe of a RP unit with its insertions is shown in figure 4.2 (left). In summary, a total of 8 identical Roman Pot units or 24 individual pots are installed in the LHC.

The single horizontal pot in each unit, placed on the radially outer side of the LHC ring, serves two purposes. Firstly, it completes the acceptance for diffractively scattered protons whose momentum loss deviates them towards this pot. On the radially inner side of the LHC ring no detector is needed since only background protons arrive in that position. Secondly, the detectors in

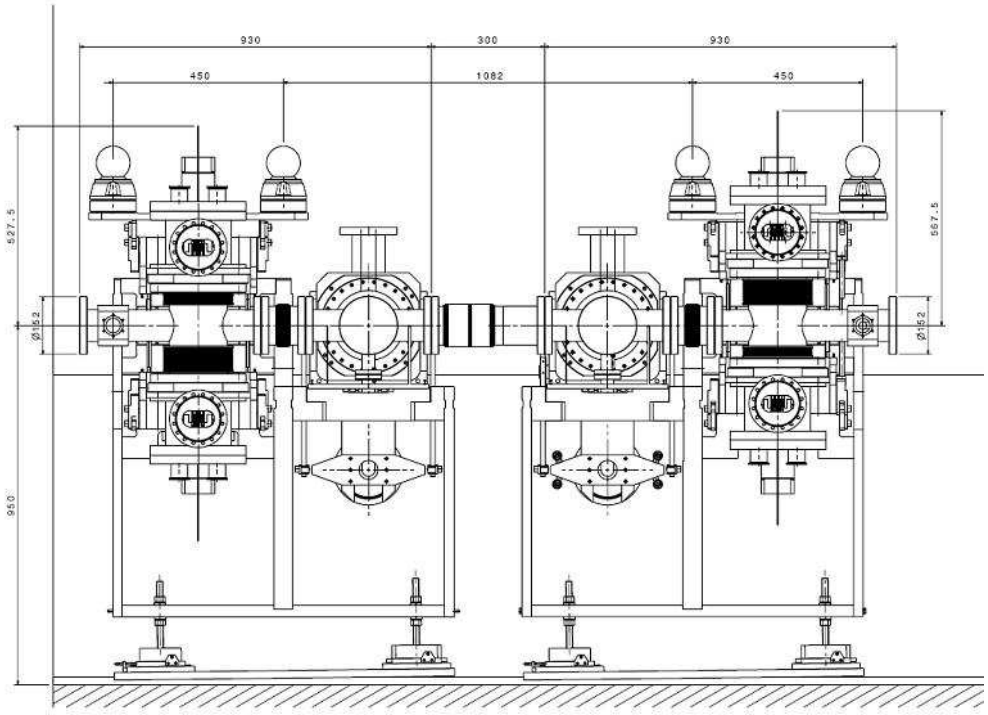

Figure 4.1: Design drawing of the station RP147, i.e. an assembly of two RP units. The other station, RP220, is identical apart from the bigger distance between the two units.

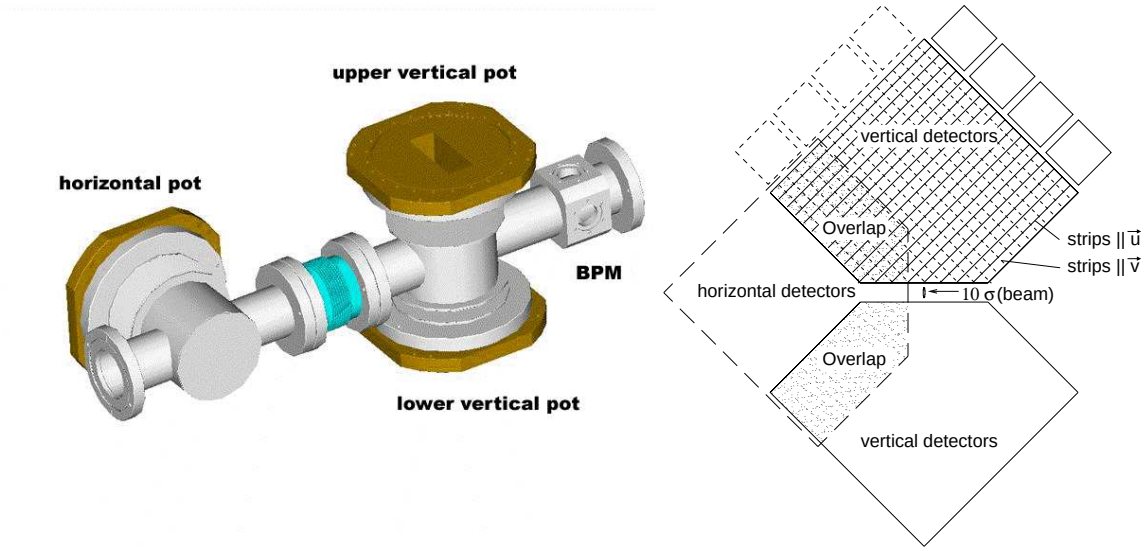

Figure 4.2: Left: the vacuum chambers of a RP unit accomodating the horizontal and the vertical pots and the Beam Position Monitor. Right: the overlap between the horizontal and vertical detectors.

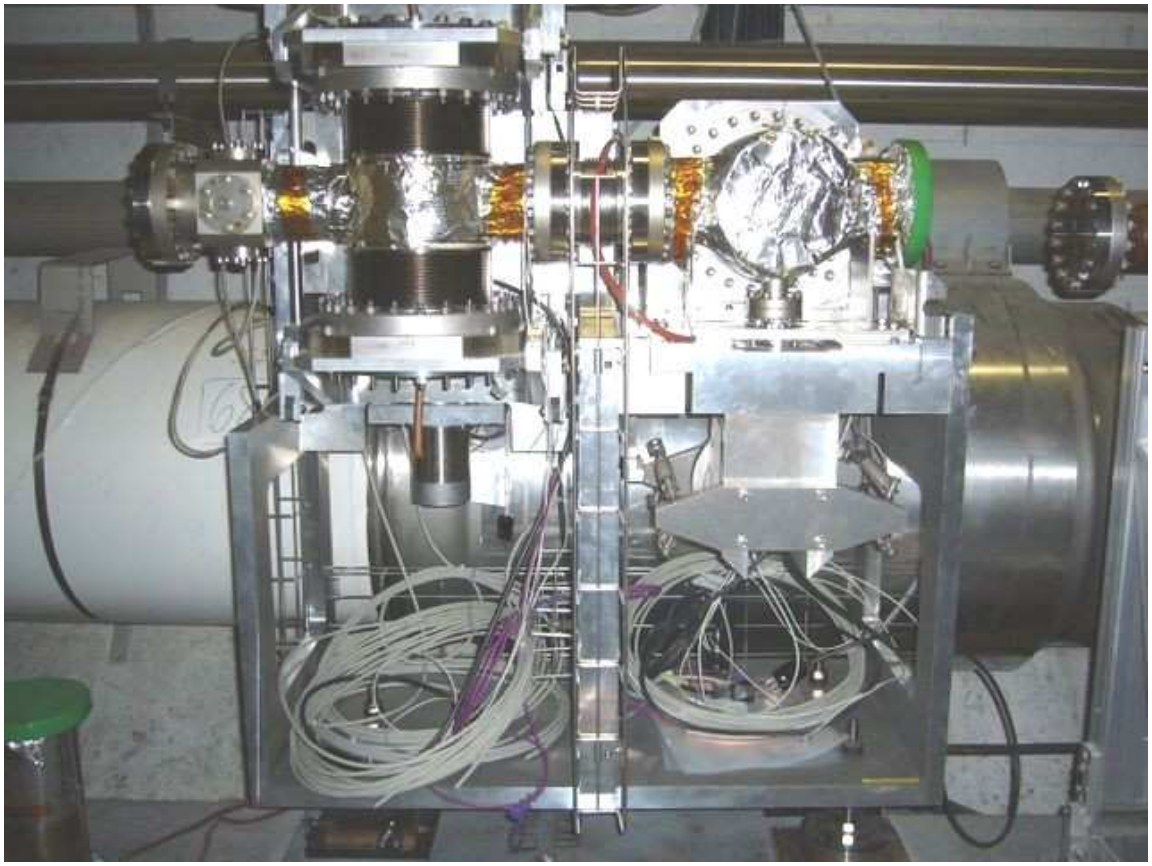

Figure 4.3: A unit of the first RP220 station installed in the LHC.

the horizontal pots overlap with the ones in the vertical pots, which correlates their positions via common particle tracks (see figure 4.2, right). This feature is used for the relative alignment of the three pots in a unit. For the absolute alignment, i.e. with respect to the beam, a Beam Position Monitor (BPM), based on a button feed-through technology, is integrated in the vacuum chamber of the vertical RP. A pre-calibration of the BPM relative to the pots is done in a metrology laboratory.

Each pot is equipped with a stack of 10 planes of novel "edgeless" silicon strip detectors (section 4.3). Half of them will have their strips oriented at an angle of $+45^\circ$ with respect to the edge facing the beam, and the other half at an angle of -45°, measuring the coordinates u and v respectively. This configuration has the advantage that the hit profiles in the two projections are equivalent. The measurement of each track projection in five planes is advantageous for the reduction of uncorrelated background via programmable coincidences, requiring e.g. collinear hits in a majority of the planes.

Figure 4.3 shows a unit of an RP220 station after installation in the LHC.

2008 JINST 3 S08007

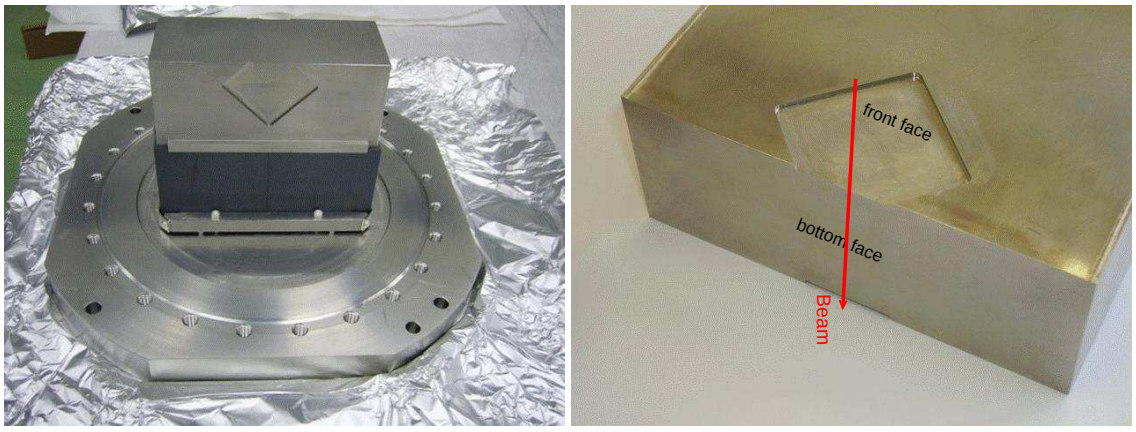

Figure 4.4: Left: the pot with the thin window and the Ferrite collar (black) needed to reduce the beam coupling impedance. Right: detailed view of the thin window; the front face is 0.5 mm thick, while the bottom face (towards the beam) is 0.15 mm thick.

4.2 Mechanical design of the Roman Pot

4.2.1 The vacuum chamber

Like all the 'warm' (i.e. non-cryogenic) vacuum equipment of the LHC, the RP vacuum chambers had to be baked out at 150°C. The supports of the two Roman pot vacuum chambers have been designed to allow a free dilatation during the bake out. Such a feature relieves the stress on the components and prevents permanent deformation. In addition, an interconnection bellow between the two vacuum chambers decouples the thermal deformations.

4.2.2 The pot and its thin window

The pot (figure 4.4) provides a volume with a secondary vacuum where the detectors and the services are enclosed. It has the shape of a 50 mm × 124 mm × 105 mm rectangular box, with 2 mm wall thickness, made of stainless steel (316LN). A support flange is attached to the box by electron beam welding. One side of the flange is connected to a bellow to close the machine vacuum volume (figure 4.5). The opposite side is connected to a second flange equipped with the detectors, which closes the secondary vacuum volume.

The RP window is composed of three parts: one facing the beam ("bottom face") and two orthogonal to the beam ("front and rear faces"). All faces have to be as thin as possible:

- The bottom face is a part of the insensitive space between the point of closest physical RP-to-beam approach and the efficient detector region. This insensitive space has to be kept small.
- The front and rear faces are traversed perpendicularly by the protons to be measured and by beam halo. To minimise signal proton deflections and showers, the window has to be kept thin.

2008 JINST 3 S08007

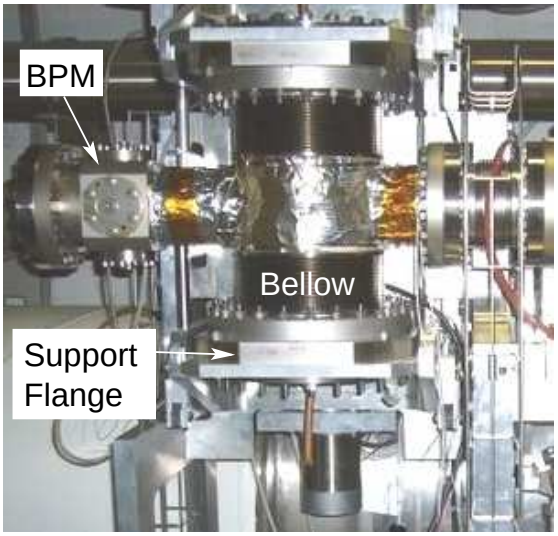

Figure 4.5: Detail of the RP220 station: the vertical pots attached to the vacuum tube by bellows.

Hence the window material, design and manufacturing technique have been optimised in view of achieving a minimum thickness and a flatness better than 50 μm, while maintaining UHV leak tightness and minimising deformations under pressure differences up to a safety-imposed limit of 1.5 bar. Comparative studies have shown that for the bottom face a thickness of 0.15 mm in stainless steel represents an optimum, while for the front and rear faces a thickness of 0.5 mm was chosen.

Several assembly procedures, like brazing, TIG and EB welding, have been investigated at CERN by the Assembly Technique group. The most satisfactory results have been obtained by brazing. The first step consists in brazing a thin window of stainless steel 316L on the bottom part of the pot. Successively the milling of the lateral sides is done, obtaining a 0.5 mm window. An excellent planarity down to 30 μm has been obtained on the prototypes.

Pressure cycles in the range $\pm$ 1 bar were applied, followed by vacuum leak tests. The maximum deformation was 0.4 mm at 1 bar, while no leaks were detected with a threshold of 2×10^{-12} mbar l/s. An ultimate hydraulic pressure test was done on two prototypes. One was loaded with a fast pressure rise, and it broke at 50 bar. The second was loaded more slowly, and the test was stopped at 80 bars without rupture (figure 4.6). For both cases, the pressure levels are many times higher than the 1.5 bar required for safety.

The pot together with the bellow creates a resonant RF cavity for the beam running along the axis of the Roman Pot. Measurements of the beam coupling impedance have been performed in the lab where a metallic wire was strung through the RP [11]. A vector network analyser generated current pulses to simulate the beam and measured the complex transmission coefficient. The bare RP (without any ferrites mounted) shows several resonances in its longitudinal beam-coupling impedance Z_L. The dominant line at 740 MHz has an impedance of 1.2 kΩ corresponding to a broad-band value $Z/n = 18\,\mathrm{m}\Omega$ with $n = f_{\mathrm{resonance}}/f_{\mathrm{LHC}}$ = 740 MHz / 11 kHz. This value was still well below but uncomfortably close to the LHC limit of $Z/n = 0.1\,\Omega$. However, a 2 mm thin collar of ferrites fixed on the external wall of the pot insertion (figure 4.4, left) removes all the resonances within the frequency domain relevant for the LHC, i.e. 0 – 1.5 GHz.

Figure 4.6: Deformation of the thin window after the ultimate pressure test, stopped at 80 bar.

4.2.3 The movements

Each pot is independently moved by micro-stepping motors with angular steps of $(0.90 \pm 0.03)^\circ$ per step, corresponding to 400 steps per turn. The transformation from the motor's rotational movement to the pot's translation movement is done by roller screws which provide high precision and zero backlashes.

A mechanical compensation system (figure 4.7) balances the atmospheric pressure load on the pot. The system relieves the stress on the driving mechanism, improving the movement accuracy and the safety of the operations. It is based on a separate vacuum system connected to the primary vacuum of the machine through a by-pass. The atmospheric pressure load on the pot-bellow system is $\sim$3000 N. With such a compensation system the stepper motor works only against the weight of the pot assembly ($\sim$100 N), leaving the possibility to achieve a better accuracy of the motor drive mechanism. With bellows on the compensation system larger than the pot bellows, a constant pulling load on the pots is guaranteed, and since the roller screws are a reversible mechanism, this feature is exploited to provide auto-retraction of the pots in case of a motor power cut.

The nominal mechanical pot-positioning resolution of the driving mechanism is 5 μm, but the final precision depends on the assembly of the motors and the roller screws. The stepper motors are equipped with angular resolvers which give the absolute position of each pot with respect to the nominal beam axis. Additional displacement inductive sensors (LVDT) provide the absolute position of each pot.

The driver units and the power supplies are placed in the counting room at up to 300 m cable distance, in a radiation protected area, where access is always possible, even with circulating beams.

4.3 "Edgeless" silicon detectors with current terminating structure

Due to their high energy, the LHC beams are very thin ($10\sigma \approx 0.8$ mm at RP220 for $\beta^* = 1540$ m). It is therefore mandatory that the silicon detectors, housed in the RPs, approach the beam centre

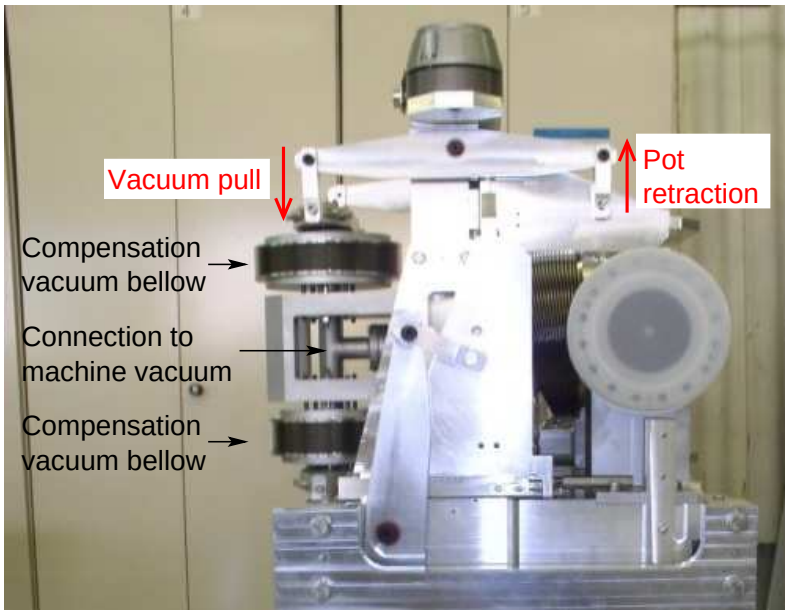

Figure 4.7: The vacuum compensation system.

to a distance as small as 1 mm. Consequently the detectors have to be fully efficient up to their mechanical edge.

Silicon detectors fabricated with standard planar technology require terminating structures to reduce electric field maxima at the detector periphery to prevent the surface irregularities on the chip cut from affecting the device performance, and to reduce the breakdown probability. They are generally a sequence of floating guardrings surrounding the sensitive part of the device and adding an external dead volume. This ring structure, called "voltage terminating structure", controls the potential distribution between the detector's sensitive area and the cut edge to have a vanishing potential drop at the chip cut. The insensitive margin increases with the number of rings, and for high voltage applications, as is the case for silicon detectors used in harsh radiation environments, it can be more than 1 mm wide. For the TOTEM experiment the reduction of this dead space is vital.

These requirements first led to tests with silicon detectors operated at cryogenic temperatures (~ 110 K, [12]) and finally triggered the development of a new terminating structure that allows detectors fabricated with standard planar technology to reach full sensitivity within less than 100 μm from the cut edge and to operate with high bias at room temperature [13].

4.3.1 The concept of current terminating structures

For segmented devices with this new so-called "Current Terminating Structure (CTS)", the potential applied to bias the device has to be applied also across the cut edges via a guardring running along the die cut and surrounding the whole sample. This external guardring, also called "Current Terminating Ring (CTR)" collects the current generated in the highly damaged region at the cut edge, avoiding its diffusion into the sensitive volume, and is separated from the biasing electrode (BE). In this manner the sensitive volume can start at less than 50 μm from the cut edge. To prevent

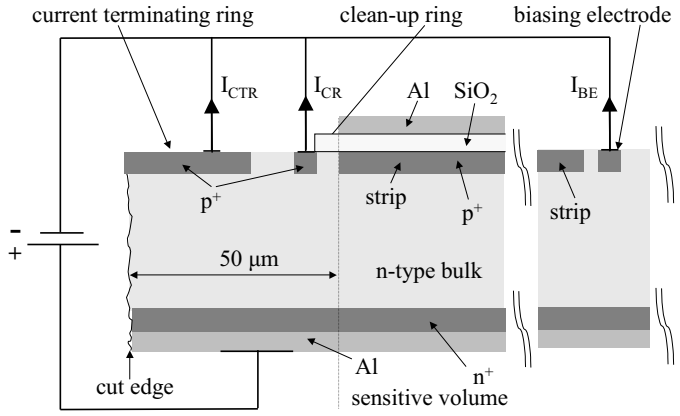

Figure 4.8: Cross-section of a silicon detector with CTS in the plane parallel to the strips and its biasing scheme.

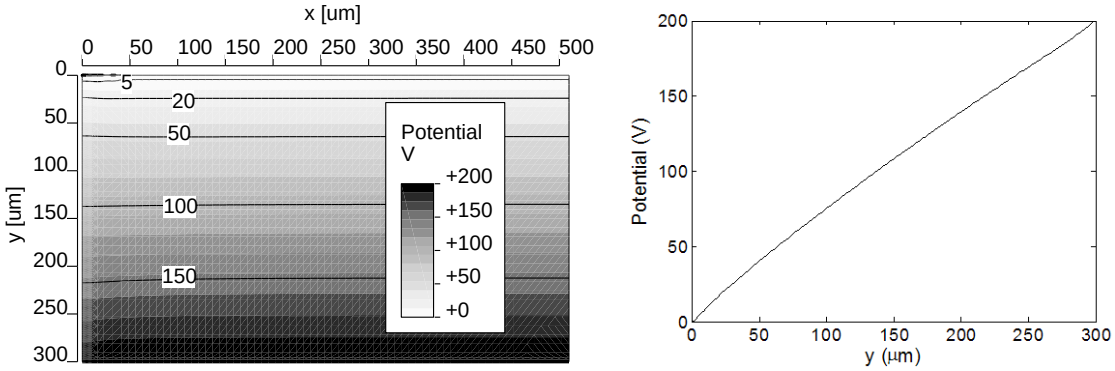

Figure 4.9: Left: potential distribution at the edge of a 300 μm thick silicon pad detector with CTS for a bias voltage of 200 V. The calculation extended up to 500 μm into the detector from the cut edge. Right: electric potential at the cut edge with an almost linear behaviour.

any further diffusion of this edge current into the sensitive volume, another implanted ring — the Clean-up Ring (CR) — can be placed between the CTR and the sensitive volume. The CTS and its biasing scheme are shown in figure 4.8.

For devices with this type of CTS, the leakage current in the sensitive volume (I_{BE}) which contributes to noise is not affected by the edge current ($I_{\mathrm{CTR}} + I_{\mathrm{CR}}$). The leakage current and the edge current have been shown to be completely decoupled. Moreover, for such devices, the charge collection efficiency has been shown to rise steeply from the edge of the sensitive volume reaching full efficiency within a few tens of micrometers (see section 4.6.1.1).

The electric potential distribution at the edge of a device with CTS has been modelled taking into account the highly damaged surface at the chip cut, where the irregularities within the first atomic layers could be assimilated to amorphous silicon. The results of this modelling have shown good consistency with the experimental results [14]. The potential distribution calculated with ISE TCAD [15] is shown in figure 4.9.

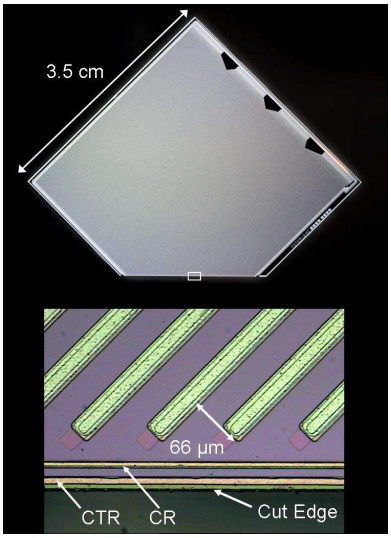

Figure 4.10: Picture of a Planar Edgeless Detector with CTS (top). The magnification of a portion of the chip cut region (bottom) shows the details of the CTS.

4.3.2 The silicon detector for the TOTEM Roman Pots

The advantages offered by the CTS have led TOTEM to choose this technology for the RP detectors. Geometry and granularity have been adapted to the specific requirements on surface coverage and spatial resolution.

The detectors have been developed and produced in a joint effort of the TOTEM group at CERN and Megaimpulse, a spin-off company from the Ioffe Physico-Technical Institute in St. Petersburg (Russia). These devices are single-sided AC p^+-n microstrip detectors with 512 strips and a pitch of 66 μm processed on very high resistivity n-type silicon wafers ($> 10\,\mathrm{k}\Omega\,\mathrm{cm}$), 300 μm thick. All of them have the CTS as described in section 4.3 on one edge, i.e. the edge facing the beam. At one end of the strips an integrated pitch adapter reduces the inter-strip distance from 66 μm to 44 μm, producing four separated groups of 128 channels. This allows direct wire bonding to the readout chip VFAT. A picture of the planar edgeless Silicon detector for the TOTEM Roman Pots and a detail of the CTS are shown in figure 4.10. In these sensors the biasing is made via "punch-through" from a biasing electrode placed inside the CR. On all the sides where the sensitivity at the edge is not required, the CTS is integrated into a standard voltage terminating structure. The strips on the detector are at an angle of 45° with respect to the edge facing the beam.

4.3.3 Electrical characterisation

For the detector polarised according to the biasing scheme shown above, the typical values of currents measured at the CTR and the CR, $I_{\mathrm{CTR}} + I_{\mathrm{CR}}$, are compared to the current measured at the biasing electrode, I_{BE}, and shown in figures 4.11 and 4.12. There is a difference of four orders of magnitude between the current at the biasing electrode flowing through the sensitive volume of the detector and the one flowing through CR and CTR. This evidences that virtually all the leakage

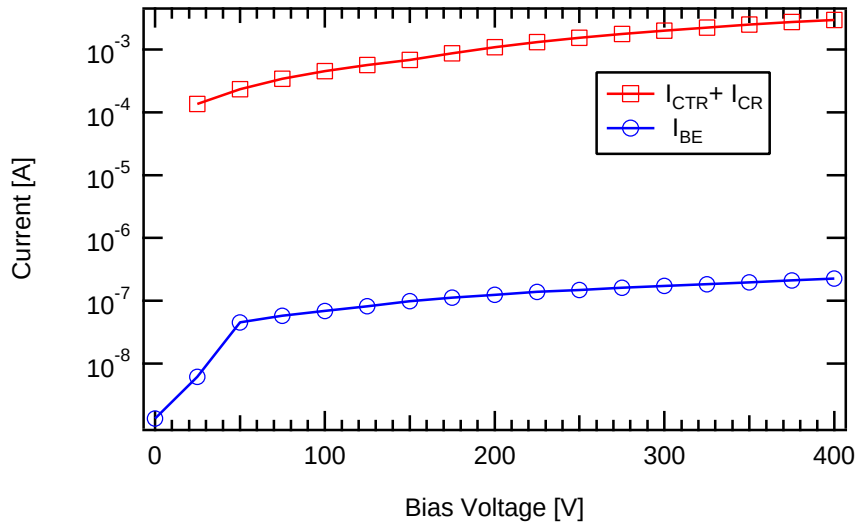

Figure 4.11: Current vs. voltage characteristics through the biasing electrode (I_{BE}) and across a detector edge ($I_{\mathrm{CTR}} + I_{\mathrm{CR}}$), measured at room temperature.

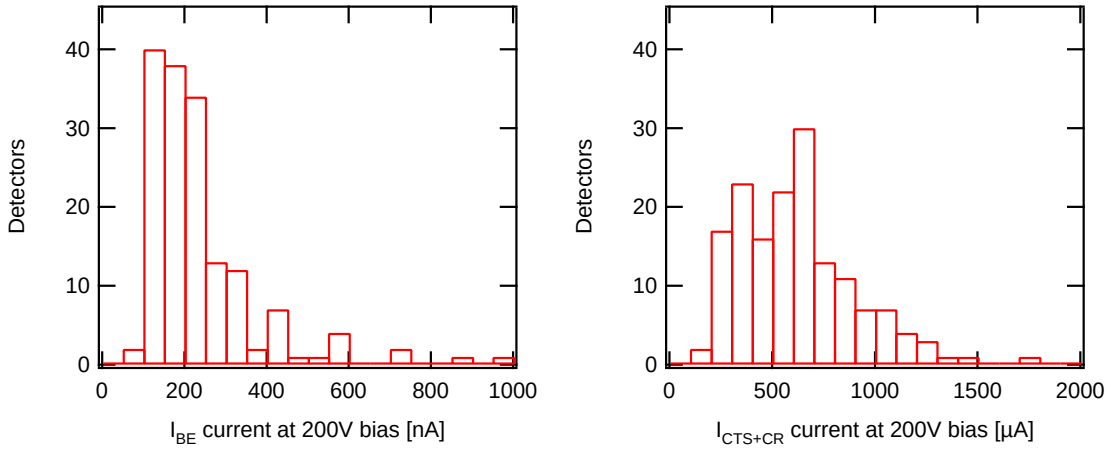

Figure 4.12: Distributions of the bulk current I_{BE} (left) and the edge current $I_{\mathrm{CTR}} + I_{\mathrm{CR}}$ (right) for a sample of 158 detectors at a bias voltage of 200 V.

current generated at the edge surface is collected by the CTR and the CR and does not flow through the sensitive volume where it would make detector operation impossible. The low current flowing into the biasing electrode confirms the validity of the current termination approach.

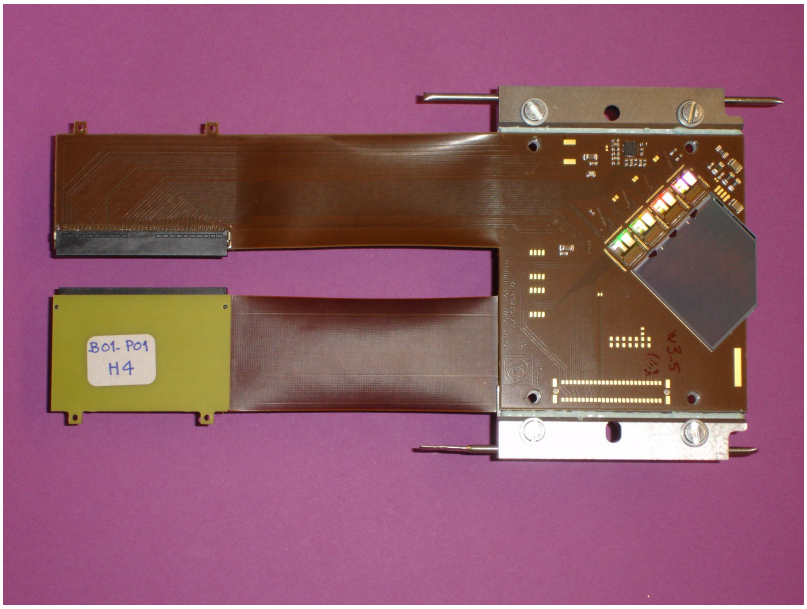

Figure 4.13: Two RP hybrids mounted back-to-back. Each hybrid carries the silicon detector and four VFAT readout chips.

4.4 On-detector electronics

The generalised electronics are described in more detail in chapter 7. Only the electronic boards that are relevant to the mechanical construction and the detector monitoring are discussed here. The silicon detector hybrid (figure 4.13) carries the detector with 512 strips wire-bonded to the input channels of 4 readout chips "VFAT" (section 7.1), and a Detector Control Unit (DCU) chip. Each VFAT provides tracking and trigger generation signals from 128 strips. The DCU chip is used to monitor detector leakage currents, power supply voltages and temperature. Via an 80 pin connector each VFAT will send the trigger outputs and the serialised tracking data from all strips to the motherboard, together with clock and trigger input signals, HV and LV power, and connections for a heater and a PT100 resistance thermometer for temperature control.

Due to the $\pm 45^\circ$ orientation of the detector strips, flipping the detector hybrid and mounting it face to face with the next one results in mutually orthogonal strips giving the u and v coordinate information. To avoid losing space in between two hybrids, all electrical components are mounted on one side such that they do not overlap for the two cards mounted face to face and that they can be separated by only one component height.

In such way 10 detector hybrids closely arranged in 5 pairs, can be connected to one motherboard feeding all electrical connections through the flange between the pot's secondary vacuum and the outside world at atmospheric pressure.

The motherboard (figure 4.14) hosts clock and trigger distribution circuitry, Gigabit Optical Hybrids (GOH) — three for data and two for trigger bit transfer, two Coincidence Chip mezzanines, LVDS-to-CMOS converters, Trigger VFAT mezzanine, Control Unit mezzanine CCUM, Radiation Monitor circuitry and temperature sensors. The binary tracking data are stored in a digital memory

2008 JINST 3 S08007

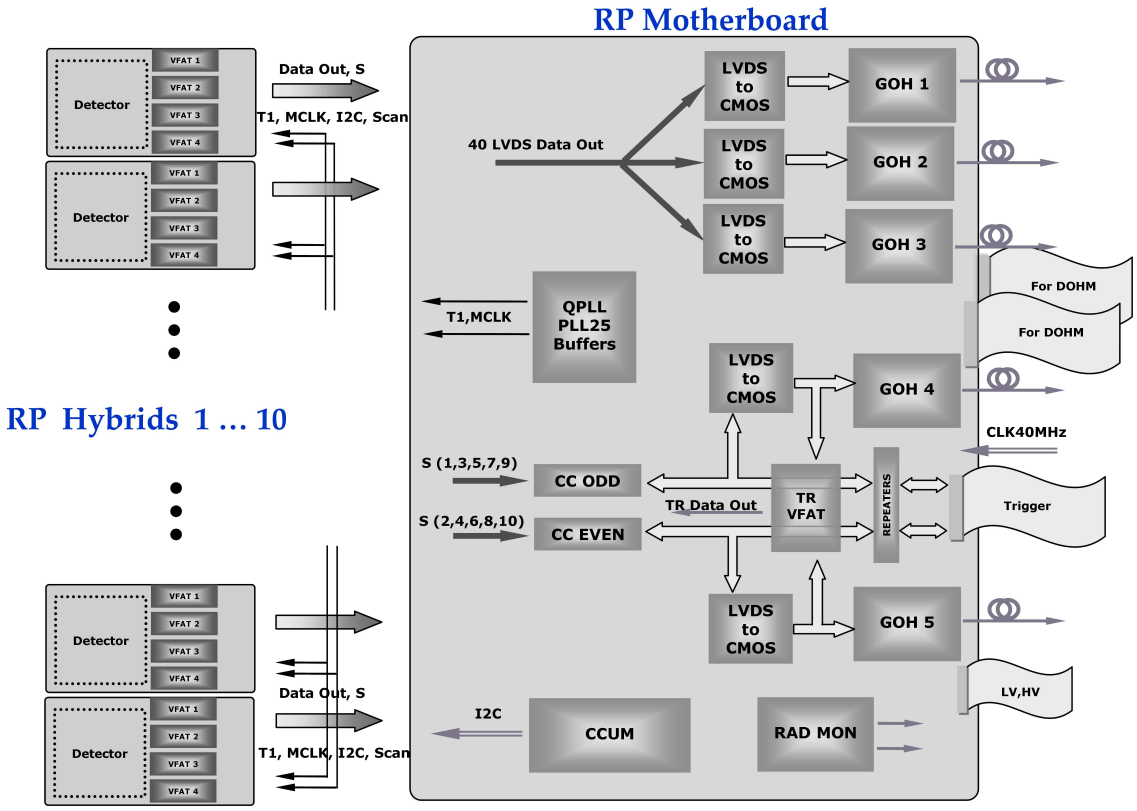

Figure 4.14: Block diagram of the RP motherboard with the connections to the hybrids.

and read out upon application of a readout trigger. A front panel with connectors for low and high voltage, control, data and trigger bit transfer to facilitates the connection to the central patch panel of the RP station.

To transmit the trigger bits to the counting room two options are implemented: the preferred choice — optical fibers — is used for the 150 m RP station and in TOTEM standalone runs also for the 220 m station. Common runs with CMS on the other hand are subject to CMS's limited trigger latency time, imposing trigger bit transmission with LVDS signals through fast electrical cables. The electrical transmission over such a long distance requires care to preserve signal integrity. This can only be achieved by restoring the LVDS signals to full levels at regular intervals over the transmission distance. A special integrated circuit was designed for this purpose: the LVDS repeater chip can treat 16 LVDS channels in parallel and was designed in special layout to guarantee radiation tolerance. This chip will be mounted on a small repeater board. At regular intervals of about 70 m a repeater station is introduced which consists of several repeater boards with cable connectors. Power for the repeaters is supplied along the cable as well, and filtered on board.

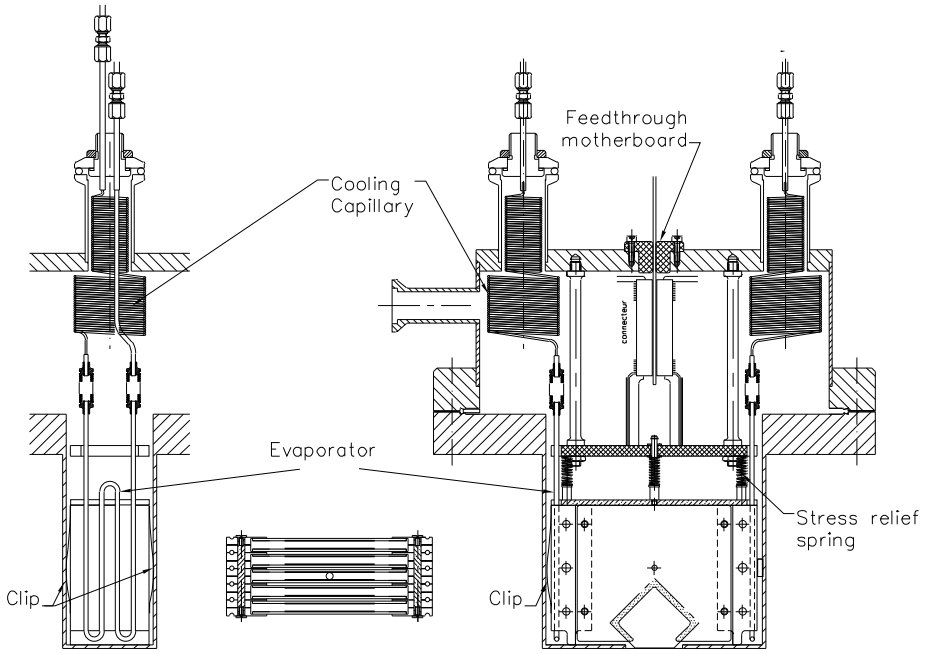

Figure 4.15: Conceptual design of the silicon detector package in the pot. In both views the clips for the alignment of the assembly are shown. The capillaries and evaporators are parts of the cooling system.

4.5 Detector integration and cooling in the Roman Pot

4.5.1 Integration of detector stacks in the pot

Each pot houses a compact stack of 10 detector planes with their hybrid boards and cooling pipes (figures 4.15, 4.16).

To keep the total width of the inefficient zone between the outer RP window surface and the active detector area below 0.5 mm, the distance between the thin window and the physical detector edge must not exceed 200 μm. The targeted alignment precision of 30 μm has to hold both at the mounting time and at the operation time. Since the detector modules will be mounted and operated at different temperatures, thermal contractions and expansions have to be taken into account.

The hybrid board is made of a processed Kapton film laminated on a high thermal conductivity substrate with a thickness of 0.5 mm. The material of the substrate is an Al-Si 70%–30% alloy (CE07), which has the advantage of a high thermal conductivity and a thermal expansion closely matching the one of the silicon sensor. The connectivity between the hybrid and the vacuum feedthrough card (motherboard) is based on a kapton 'pigtail' with end connector. Both the silicon sensor and the four VFAT chips are glued with thermally conductive thermoplastic film to the hybrid. The chips are aligned on the hybrid using precision markers. After bonding the outputs of the chips to the hybrid the proper functioning of the complete hybrid is tested. In a second step, the sensor is aligned such that the bond pads of chips and sensor are best matched, and the input side of the chips is then bonded to the sensor. No special tools, except a bonding jig are required up to this point. Ten completed hybrids are then assembled by means of precision dowels and micrometre

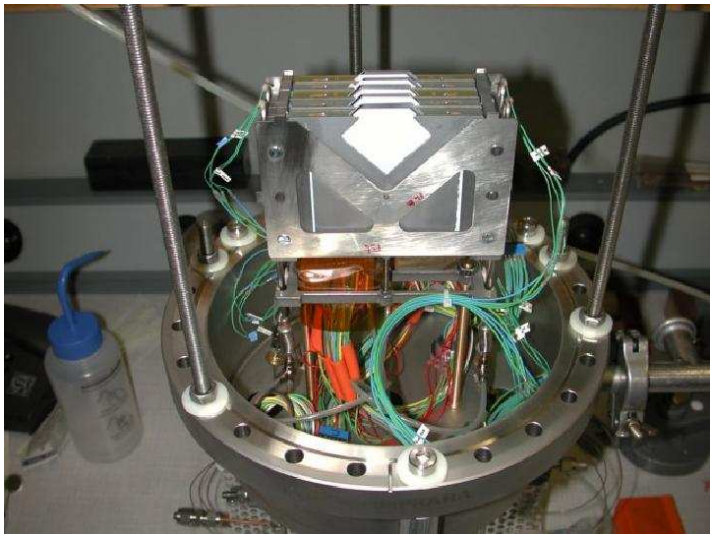

Figure 4.16: The detector package prototype mounted on the vacuum chamber.

stages to form the detector package. Survey with a 3D Coordinate Measuring Machine (CMM) is performed to determine the edge locations of all ten silicon sensors.

The assembly is fixed by means of a slightly flexible fixation on the support plate which is rigidly attached to the detector vacuum flange. The fixation is spring loaded. Once the detector is inserted in the Roman Pot, it exerts a small force on the bottom plate of the Pot ensuring the positioning of the assembly relative to the bottom plate. A flexible clip on the side of the assembly maintains the assembly with a slight force aligned to one side wall of the pot. A second similar clip will ensure the alignment of the assembly with respect to the front and back walls. The entire structure is conceived such that it can be dismantled and reassembled.

4.5.2 The cooling system

The cooling system integrated in the RP insertion will have to remove the thermal load from the sensors and the electronics. Moreover, to allow operation after high irradiation the RP silicon detectors will be operated at about -10°C to reduce the radiation induced thermally generated bulk current and to control the reverse annealing after high irradiation. Nevertheless given the geometry of the package it will be difficult to keep all modules at the same temperature. A spread of less than 10°C between the ten plates can be tolerated and does not represent a strong constraint. The major contribution to the thermal load of the whole system is given by the readout chips (VFATs). The total load per pot is about 20 W.

Because of the high radiation environment of the LHC tunnel, the main part of the refrigeration system is not installed near the RP but in the underground service area USC55 at IP5, a protected and always accessible place.

An evaporative fluorocarbon cooling strategy [16] has been adopted since it can transport fluid at ambient temperature over long distances (from USC55 near IP5 to the RP stations at 147 m and 220 m) without heat losses but only pressure drops which are still low and can be balanced by the compressors. The throttling of the fluid is done in the pot and is based on metal capillary

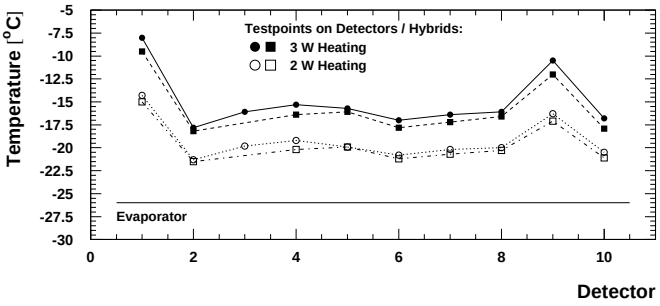

Figure 4.17: Temperature distribution measured on testpoints on the detectors (circular markers) and on the hybrids (square markers) for a heating power of 2 W and 3 W (open and solid markers respectively), compared with the evaporator temperature.

tubes. The C_3F_8 fluorocarbon dielectric fluid has been selected because it is non-flammable, non-conductive and radiation resistant. The heat transfer process is very effective because of the two phase flow regime.

The evaporative cooling system has been designed to guarantee a total cooling capacity of 1.2 kW and supply a global mass flow rate of 40 g/s to be uniformly shared between the 24 TOTEM Roman Pots. The fluid is supplied in liquid phase and at high pressure at the RP circuit inlet. The system is completely oil free and the process fluid adequately filtered to avoid any mechanical particle obstructing the lamination capillaries' inner section under irradiation.

Inside the Roman Pot the fluid medium flows through thin-walled copper-nickel pipes of 2.5 mm outer diameter. Two independent pipe evaporators supply fluid to the right and left side of the detector package. The evaporators are mechanically decoupled from the detector assembly at the inputs and outputs either by a bellow or by a spiral section. They are shaped in a double-S configuration and are squeezed in between the frame structure which foresees precisely machined grooves for this purpose. The evaporators are fed by capillary tubes that provide the throttling of the fluid. The coolant in gas phase is exhausted via larger diameter pipes. Both the capillaries and the exhausting pipes enter and leave the pot through two vacuum feed-throughs.

4.5.3 Tests on the thermo-mechanical prototype

A thermo-mechanical prototype has been assembled to characterise the conceptual design, the choice of the materials and the fluido-dynamic parameters of the cooling system. The VFAT chips on the hybrids were replaced with heaters with equivalent power density. The prototype was fixed to a vacuum chamber flange and inserted in an experimental vacuum chamber. All the connections of the pressure and temperatures sensors were read out through the vacuum feed-through. A capillary tube with an inner diameter of 0.55 mm was used.

The measurements showed that for the expected heating power of 2 W the temperature spread on a single hybrid card is within 3°C, and the maximum temperature difference between detectors is less than 10°C (figure 4.17).

The final length of the capillary, 1.5 m, is the result of an optimisation in view of obtaining a suitable pressure drop. The capillary will be coiled up in the pot to minimise the heat loss and the need of additional insulation.

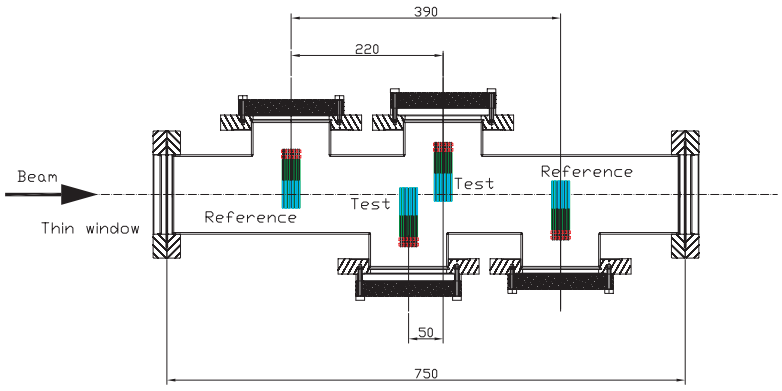

Figure 4.18: Arrangement of the test detectors and reference detectors with respect to the beam axis (dashed line) inside a test vacuum tube.

4.6 Detector performance

4.6.1 Detector tests with analog readout

4.6.1.1 Testbeam measurement of CTS detector performance

Edgeless silicon detectors have been tested in autumn 2004 with a muon beam in the SPS X5 area at CERN [13, 17]. The sensors had the final size and strip pitch of 66 μm. They were assembled into 4 packages each consisting of 8 detectors. The majority was read out with CMS's analogue APV25 chips [18] while a few were equipped with prototypes of TOTEM's own front-end chip, the VFAT, to test its trigger functionality. The packages formed a telescope placed inside a vacuum tube (see figure 4.18).

The outermost assemblies were used as reference to define tracks while the inner ones served as devices under test. The detector positions were measured with a precision of a few tens of microns. In the data analysis, the detector alignment was further refined with a global χ^2 minimisation algorithm to the precision of the order of 1 μm.

The detector setup was used to determine the resolution and the behaviour of the efficiency at the active edge of the test detectors. For these studies the detectors were operated at a temperature of around -10°C.

The CTS detectors in the test setup were biased at of 50 V, enough to overdeplete them and allow the full charge collection within the integration time of the readout electronics. Since more than 80% of hit clusters in these detectors consisted of one strip, the resolution of the detectors was close to the theoretical result when charge sharing is negligible, which is given by $d/\sqrt{12} = 19\,\mu$m, where $d = 66\,\mu$m is the strip pitch. A typical residual distribution is shown in figure 4.19 (left).

The efficiencies of the test detectors with respect to their geometrical coordinates were computed as fractions of accepted tracks. A track was considered as accepted when the test detector registered a hit within $\pm 100\,\mu$m from the track. The combined reconstruction and alignment information was used to determine the position of the cut detector edges. The observed 10%–90% efficiency rise interval at the active edge was for all detectors smaller than 50 μm, and the re-

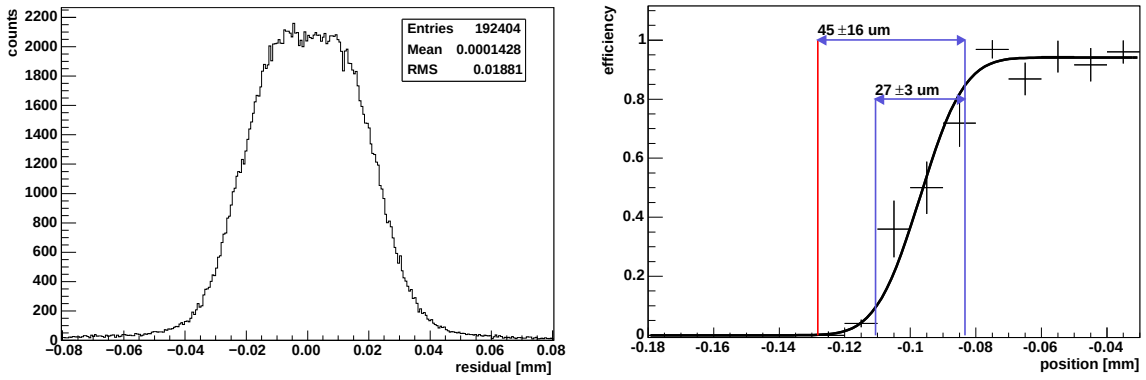

Figure 4.19: Left: residual distribution of a CTS test detector. The observed resolution was about 19 μm for all the test detectors, as expected from theory. Right: the efficiency of a CTS detector at the sensitive edge. The left-most vertical line indicates the reconstructed position of the physical edge, the other two vertical lines indicate the 10%–90% efficiency rise interval. The fit was performed with a Gaussian error function.

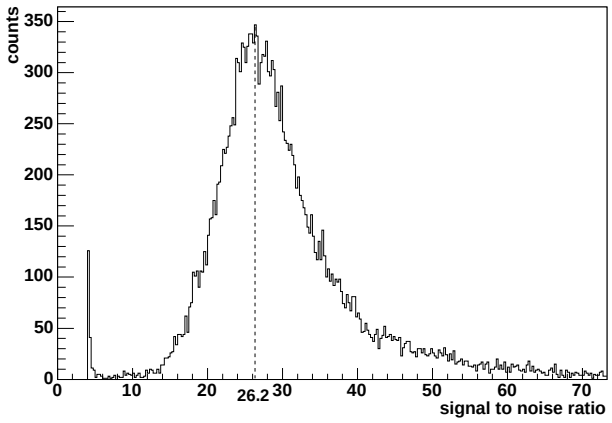

Figure 4.20: Signal-to-noise ratio distributions of a CTS test detector operated at a bias voltage of 100 V and at -11°C. The value of the most probable signal-to-noise ratio equals 26.2.

constructed distance between the cut edge and the position where 90% efficiency is reached was smaller than 60 μm. Figure 4.19 (right) shows the behaviour of the efficiency of one of the test detectors along the direction perpendicular to the cut edge.

Depending on the bias voltage and the detector thickness, the most probable value of signal-to-noise ratio was between 20 and 30. Figure 4.20 presents an example signal-to-noise distribution of the over-depleted test detector, operated at the bias voltage of 100 V.

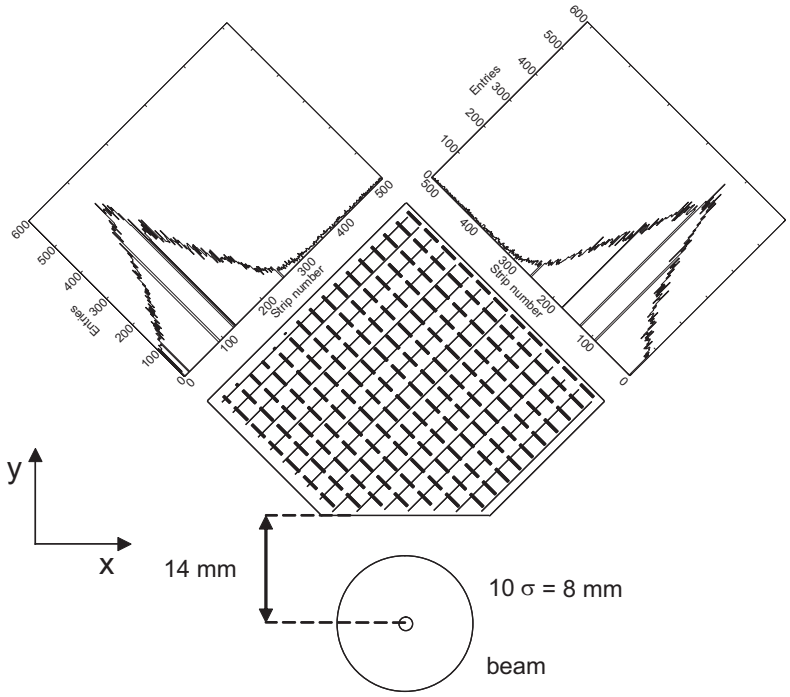

Figure 4.21: Profile of the SPS beam halo as seen by two orthogonal CTS detector planes at a distance of 14 mm from the beam centre. The data were taken with the bottom pot and the picture has been rotated by 180° around the beam axis for more convenience.

4.6.1.2 Full RP operation test in the SPS accelerator

The full operation of a Roman Pot unit prototype, consisting of a vacuum chamber equipped with two vertical insertions, was tested in a coasting beam experiment in the beamline of the SPS accelerator at CERN [11]. Each of the two insertions hosted four pairs of edgeless silicon detectors mounted back to back. In this early test, three pairs in each pot were used for tracking and were read out with the analogue APV25 chips. One pair was read out with a first prototype version of the digital VFAT chips delivering the fast-OR signal of all 512 strips used for triggering the data acquisition system in coincidence with the sum signal of the four pick-up electrodes of a beam position monitor located close to the detectors. Three different bunch structures were tested in the SPS accelerator: 1 single bunch in the accelerator ring, 4 bunches equally spaced, and 4 equally spaced trains of 4 bunches of 8×10^{10} 270 GeV protons with a revolution period of 23 μs. Detector data were taken with the two pots moving independently between 6 mm and 14 mm ($\sigma_{\text{beam}} = 0.8$ mm) from the beam pipe centre. Beam halo protons were detected at typical rates of 3 kHz. Figure 4.21 shows the halo profiles measured by two orthogonal detector planes of this pot. There were a few noisy channels on both detectors which have been removed from the profiles.

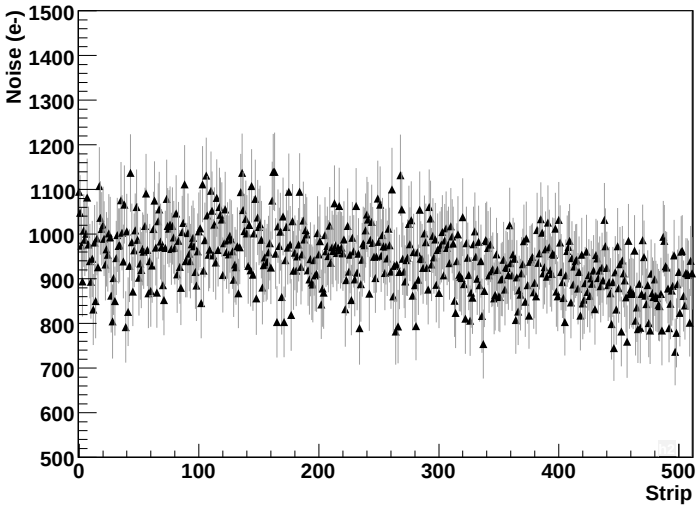

Figure 4.22: Noise at the different VFAT channels bonded to the edgeless detector biased with 150 V.

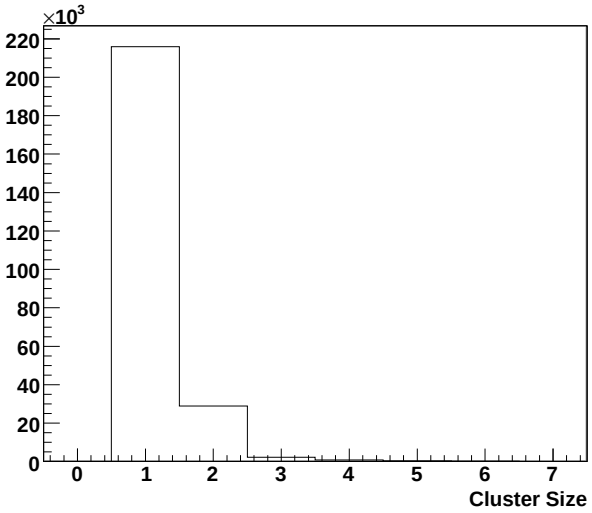

Figure 4.23: Cluster size in number of strips for particles perpendicular to the detector plane (detector bias: 150 V).

4.6.2 Operation of CTS detectors with VFAT chip

During 2007, the silicon detectors with CTS were tested in the H8 beam with the final electronics. Each detector was mounted on a final hybrid as described in section 4.4. Figure 4.22 shows the noise per strip, expressed in electrons, for all strips of one detector. The average noise and the rms are about 1000 and 100 electrons respectively. No outstandingly noisy channels were observed.

Tracks were defined in the H8 beam with a small size scintillator hodoscope, adjusted to the beam size. The cluster size for tracks, perpendicular to the test detector plane, is plotted in figure 4.23. In 90% of the cases, the cluster contains only 1 strip. This is a typical scenario for the forward protons in the TOTEM experiment since they are parallel to the beams and hence perpendicular to the detector planes within better than 1 mrad.

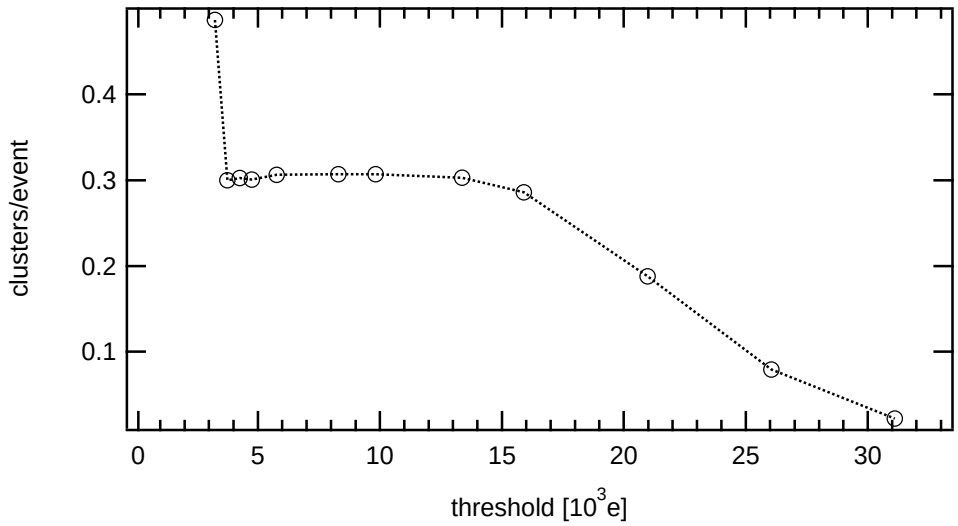

Figure 4.24: Threshold scan for one of the four VFAT chips of the Roman Pot Hybrid performed with a pion beam from the SPS. The number of clusters per triggered event is plotted versus the discriminator threshold expressed in electrons (detector bias: 150 V). The trigger was given by two scintillators in coincidence whose overlap covered slightly less than the whole CTS detector, about 3 times the area read out by the VFAT considered here, which explains the plateau level of $\sim 30\%$.

In order to demonstrate the detector response, several threshold scans were performed with a pion beam. In figure 4.24 the number of clusters per triggered event is plotted versus the discriminator threshold expressed in electrons. The noise starts to become visible at a threshold of 3000 electrons (three times above the average noise, see figure 4.22), at an occupancy level of 0.2% per strip. The wide plateau extends over a range of 10000 electrons. The maximum of the pulse height distribution can be estimated from the falling edge of the threshold curve. It corresponds to an efficiency loss of about 1/3 at a threshold of 21000 electrons, resulting in a signal-to-noise ratio in the range of 20 to 25.

4.6.3 Irradiation studies for CTS detectors

It is important to evaluate the radiation hardness of the edgeless Silicon detectors. However, there are no indications to believe that the performance of the edgeless devices with CTS after high radiation would degrade faster than the ones with standard voltage terminating structures provided that the edge current ($I_{\mathrm{CTR}} + I_{\mathrm{CR}}$) and the sensitive volume current (I_{BE}) whose dominant component is the bulk current, remain decoupled also after high radiation. To prove this assumption, edgeless silicon detectors have been irradiated at the neutron reactor TRIGA in Ljubljana at different fluxes up to 10^{14} $1\,\mathrm{MeV\,n/cm^2}$. The edge current stays constant, independent of the radiation dose (figure 4.25, left). The bulk current I_{BE} increases proportional to the fluence Φ (figure 4.25, right). The damage factor α, defined as

$$\alpha = \frac{I_{\mathrm{BE}}}{\mathscr{V}\Phi}\,, \tag{4.1}$$

where $\mathscr{V}$ is the detector volume, amounts to about $5 \times 10^{-17}\,\mathrm{A/cm}$ [19], which is in agreement with earlier measurements on devices using standard voltage terminating structures [20].

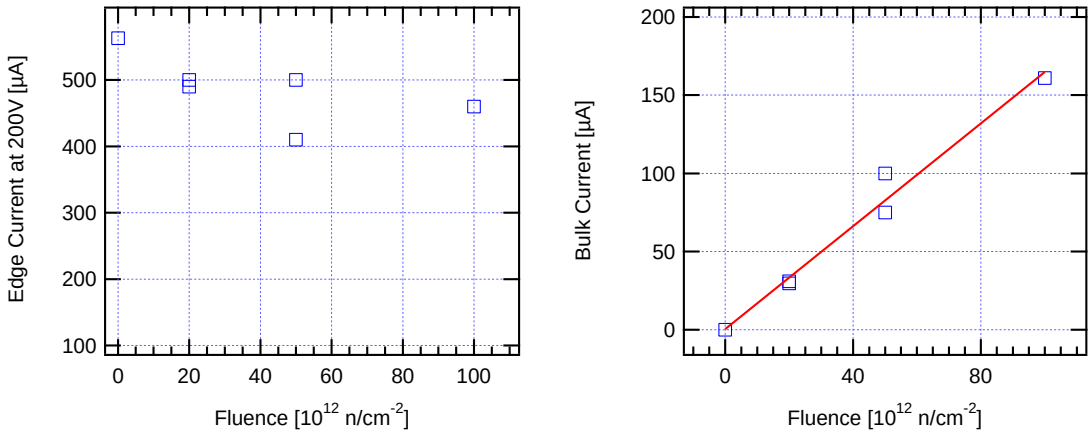

Figure 4.25: Left: edge current of CTS detectors biased at 200 V after different neutron fluences. Right: bulk current at full depletion voltage as a function of the fluence fitted with a linear function.

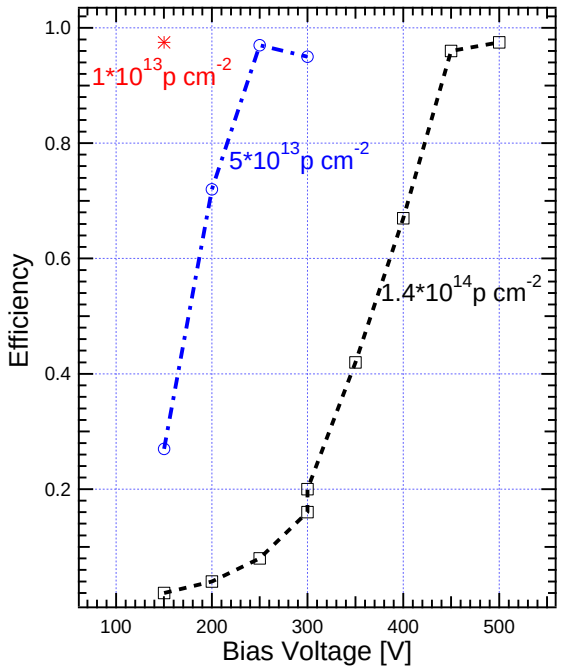

Figure 4.26: Efficiency of irradiated Edgeless Detectors with CTS at the working temperature of -18°C. The efficiency has been calculated by comparing the hits in the irradiated detector with the hits in a non-irradiated detector placed in front, along the beam axis.

More detectors have been irradiated with 24 GeV protons at CERN. The efficiency of these detectors as measured in the H8 test beam is given in figure 4.26 as a function of the bias voltage. Whilst a radiation up to $10^{13}\,\mathrm{p/cm^2}$ does not change the detector behaviour, stronger irradiated detectors ($1.4 \times 10^{14}\,\mathrm{p/cm^2}$) need a much higher bias voltage up to 450 V to be fully efficient. Presently, a radiation of $10^{14}\,\mathrm{p/cm^2}$ is considered as an upper limit for a functioning detector.

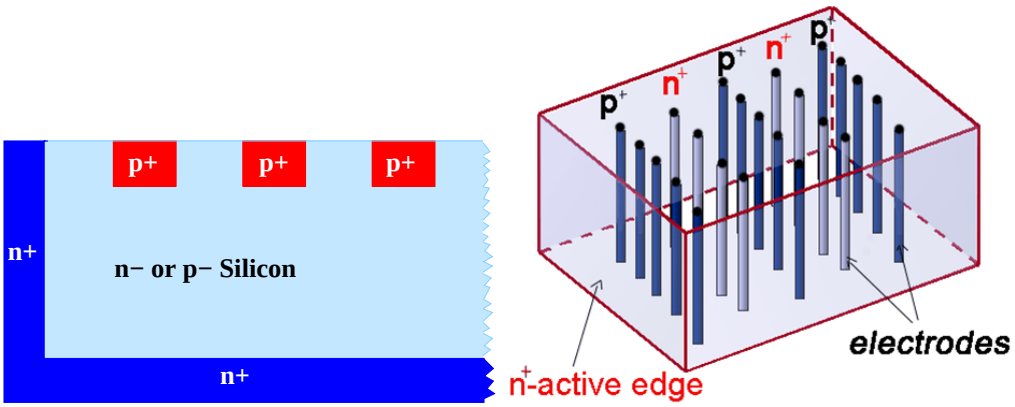

Figure 4.27: Left: sketch of a planar-3D detector. The edge (dark region) on the left hand side of the sketch, is an extension of the backside n^+ electrode and allows full control of the electric field lines at the edge. Right: sketch of a full 3D detector where the p^+ and n^+ electrodes are processed inside the silicon bulk. The edges constitute another n^+ electrode surrounding the 3D volume.

The above detectors were homogenously irradiated whereas in the experiment, due to diffractive protons, only a tiny area of a few mm^2 close to the sensitive edge is exposed to high proton fluence. Therefore, a non-irradiated detector was tested with bias voltages up to 500 V. Performance problems at this large bias voltage were not observed. However, a few strips showed a higher noise occupancy than at lower voltages.

Calculations of the diffractive proton flux hitting the detectors indicate that the present detectors will probably be alive up to an integrated luminosity of about $1\,fb^{-1}$. To cope with higher luminosities, TOTEM has initiated an INTAS project [21] to develop radiation harder edgeless detectors.

4.7 Alternative detector technologies: planar-3D and full 3D silicon

In addition to the planar silicon detectors with CTS, TOTEM is considering to equip some RPs partly with another novel type of "edgeless" silicon detectors: the planar-3D detectors [22], i.e. devices with a conventional planar microstrip interior and active edges as introduced with the full 3D detector technology [23]. In this configuration, the free edges of a planar detector are deep etched and n^+ dopant diffused in. Then the sensor is removed from the wafer again by etching, avoiding in this way the typical surface defects produced by saw cuts. In this way the edges of the sensor become an extension of the back-side n^+ electrode to the front side, as shown schematically in figure 4.27 (left). This enclosing n^+ electrode — the "active edge" — completely defines the electric field lines when a reverse bias voltage is applied. Also with this technology, the dead area which would be needed for guard rings in conventional planar detectors is reduced to no more than a few tens of microns.

Prototypes of planar-3D detectors have been tested in the 2004 testbeam together with the CTS detectors. Both the efficiency rise at the edge and the spatial resolution of the planar-3D detectors were measured to be very similar to those of the CTS detectors. However, these early

sensor prototypes had only a thickness of 235 μm and — due to a production problem — could only be biassed with voltages up to 30 V where they are not yet fully depleted. Both facts led to a most probable signal-to-noise ratio of only 11.5. Studies on more advanced samples of this detector technology are being continued.

On the quest for edgeless radiation-hard detector technologies, TOTEM has also conducted the first beamtest with small prototypes of full 3D active-edge detectors, as sketched in figure 4.27 (right) and described in [23]. The test results were very encouraging [24]. In particular, the 10-to-90% efficiency rise at the edge happens over a distance of only 18 μm, and the measured sensitive width of the detector is equal to the physical width within 10 μm. While the production of large-area sensors is still difficult at present, this intrinsically radiation-hard technology [25] is a promising upgrade option for future operation at highest luminosities.